Research Square

Preprints are preliminary reports that have not undergone peer review.
They should not be considered conclusive, used to inform clinical practice,
or referenced by the media as validated information.

Simulating Chern insulators on a superconducting quantum processor

Heng Fan (hfan@iphy.ac.cn)
Institute of Physics, Chinese Academy of Sciences https://orcid.org/0000-0002-5328-2449

Zhongcheng Xiang
Institute of Physics, Chinese Academy of Sciences

Kaixuan Huang
Institute of Physics, Chinese Academy of Sciences

Yu-Ran Zhang
RIKEN https://orcid.org/0000-0002-6893-2053

Tao Liu
South China University of Technology

Yun-Hao Shi
Institute of Physics, Chinese Academy of Sciences https://orcid.org/0000-0003-1130-4280

Cheng-Lin Deng
Institute of Physics, Chinese Academy of Sciences

Tong Liu
Institute of Physics, Chinese Academy of Sciences

Hao Li
Institute of Physics, Chinese Academy of Sciences

Gui-Han Liang
Institute of Physics, Chinese Academy of Sciences

Zheng-Yang Mei
Institute of Physics, Chinese Academy of Sciences

Haifeng Yu
Beijing Academy of Quantum Information Sceinces

Guangming Xue
Beijing Academy of Quantum Information Sciences

Ye Tian
Institute of Physics, Chinese Academy of Sciences

Xiaohui Song
Institute of Physics, Chinese Academy of Sciences

Zhi-Bo Liu
Nankai University

Kai Xu

Institute of Physics, Chinese Academy of Sciences https://orcid.org/0000-0002-7776-2455

Dongning Zheng

Institute of Physics, Chinese Academy of Sciences

Franco Nori

RIKEN https://orcid.org/0000-0003-3682-7432

Article

Keywords:

Posted Date: September 22nd, 2022

DOI: https://doi.org/10.21203/rs.3.rs-1968982/v1

License: This work is licensed under a Creative Commons Attribution 4.0 International License.
Read Full License

Simulating Chern insulators on a superconducting quantum processor

Zhong-Cheng Xiang,[1,*] Kaixuan Huang,[1,6,5,*] Yu-Ran Zhang,[2,3,*] Tao Liu,[4] Yun-Hao Shi,[1] Cheng-Lin Deng,[1] Tong Liu,[1] Hao Li,[1] Gui-Han Liang,[1] Zheng-Yang Mei,[1] Haifeng Yu,[5] Guangming Xue,[5] Ye Tian,[1] Xiaohui Song,[1] Zhi-Bo Liu,[6] Kai Xu,[1,5,7,8,†] Dongning Zheng,[1,7,8] Franco Nori,[2,3,9,‡] and Heng Fan[1,5,7,8,§]

[1]*Institute of Physics, Chinese Academy of Sciences, Beijing 100190, China*
[2]*Theoretical Quantum Physics Laboratory, RIKEN Cluster for Pioneering Research, Wako-shi, Saitama 351-0198, Japan*
[3]*RIKEN Centre for Quantum Computing (RQC), Wako-shi, Saitama 351-0198, Japan*
[4]*School of Physics and Optoelectronics, South China University of Technology, Guangzhou 510640, China*
[5]*Beijing Academy of Quantum Information Sciences, Beijing 100193, China*
[6]*Key Laboratory of Weak Light Nonlinear Photonics, Ministry of Education, Teda Applied Physics Institute and School of Physics, Nankai University, Tianjin 300457, China*
[7]*CAS Centre for Excellence in Topological Quantum Computation, UCAS, Beijing 100190, China*
[8]*Songshan Lake Materials Laboratory, Dongguan 523808, China*
[9]*Physics Department, University of Michigan, Ann Arbor, Michigan 48109-1040, USA*

The quantum Hall effect, fundamental in modern condensed matter physics, continuously inspires new theories and predicts emergent phases of matter [1, 2]. Analysing Chern insulators, a lattice version of the quantum Hall effect without external magnetic field, by testing the bulk-edge correspondence [3] remains challenging on quantum simulation platforms [4]. Here we experimentally demonstrate three types of Chern insulators with synthetic dimensions [5, 6] on a programable 30-qubit-ladder superconducting processor. Using a dynamic spectroscopic technique, we directly measure the band structures of the 2D Chern insulator along synthetic dimensions with various configurations of Aubry-André-Harper chains [7, 8]. By monitoring the quantum walks of an excitation initialised at the edge qubit, we observe dynamical localisation of the topologically protected chiral edge states. With these two signatures of topology, our experiments implement the bulk-edge correspondence in the synthetic 2D Chern insulator. Moreover, we simulate two different bilayer Chern insulators on the ladder-type superconducting processor. With the same periodically modulated on-site potentials for two coupled chains, we observe topologically nontrivial edge states with zero Hall conductivity [9]. When the on-site potentials of two coupled chains have opposite signs, we probe a Chern insulator with higher Chern numbers [10–12]. Our work shows the potential of using superconducting qubits for investigating different intriguing topological phases of quantum matter.

Topological phases of matter [1, 2], classified beyond Landau's symmetry-breaking theory, have been attracting growing interest in recent decades. It started with the discovery of the two-dimensional (2D) integer quantum Hall effect (QHE) [13], which arises from the topological nature of Bloch bands characterised by the Chern number [14]. Topological band theory provides a direct link between theory and experiments, which are successful for identifying salient characteristics of topological states and predicting new classes of topological phases [3]. The existence of robust edge states is deeply related to the topology of gapped bulk band structures, which is the ubiquitous bulk-edge correspondence in topological systems. Since exploring higher-dimensional physics requires an exponentially growing number of qubits, there is growing interest in creating synthetic dimensions to construct a higher-dimensional lattice in a lower-dimensional system with its internal degrees of freedom [5, 6, 15, 16]. Moreover, a lower-dimensional topological charge pump shares the same topological origin as higher-dimensional topological physics, e.g., a one-dimensional (1D) Thouless pump for the 2D integer QHE [17] and a 2D topological pump for a four-dimensional quantum Hall system [18, 19]. In addition to the 2D electron gas, the integer QHE and Chern insulators (i.e., a lattice version of the QHE) have also been observed in other physical platforms, including ultra-cold atoms in optical lattices [20–22], photonic systems [23–25], etc. [26, 27]. However, it still remains very challenging to synthesise topological quantum phases and to further demonstrate the bulk-edge correspondence in quantum simulation platforms [4, 28, 29].

Here we observe several topological signatures of 2D and bilayer Chern insulators with synthetic dimensions on a programable 30-qubit-ladder superconducting processor. We experimentally measure the band structure of the 2D Chern insulator along a synthetic dimension by analysing the temporal frequency of the system's response to local perturbations. By monitoring quantum walks (QWs) of a single excitation initially prepared at an edge qubit, we demonstrate dynamical localisation of the topologically protected edge states. The measured band structure and the dynamical signatures of topological edge states together demonstrate the *bulk-edge correspondence*. Furthermore, we synthesise two different bilayer Chern insulators on the 30-qubit-ladder processor. Given the same periodically modulated on-site potentials of two coupled chains, we probe the nontrivial topological edge states with *zero* Hall conductivity. When on-site potentials of two coupled chains have opposite signs, a Chern insulator with *higher* Chern numbers is probed. Our results show that superconducting simulation platforms are capable for studying different intriguing topological phases of quantum matter.

Experimental setup and model Hamiltonians

Our experiments are performed on a superconducting circuit

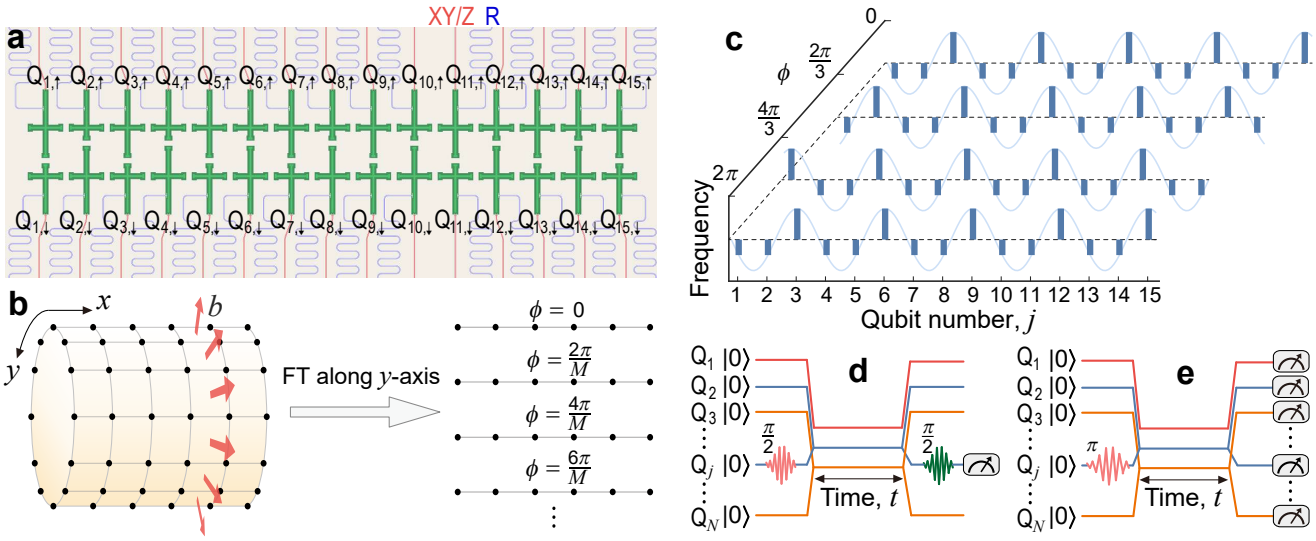


Fig. 1. **Quantum simulation of Chern insulators on a 30-qubit-ladder superconducting processor. a**, Schematic of the superconducting quantum processor, where 30 superconducting qubits constitute a ladder. Each qubit, coupled to an independent readout resonator (R), has an independent microwave line for XY and Z controls. **b**, Mapping the 2D Hofstadter model to various configurations of Aubry-André-Harper (AAH) chains with a Fourier transformation (FT) along the y-axis with M sites. **c**, Qubits' frequencies for the synthesis of a series of AAH chains with different values of ϕ and $b = \frac{1}{3}$. **d**, **e**, Experimental waveform sequences for the dynamic band structure spectroscopy (**d**) and the single-particle quantum walks (QWs) (**e**).

[30] consisting of 30 transmon qubits ($Q_{j,s}$, with j varied from 1 to 15 and pseudo-spin $s \in \{\uparrow, \downarrow\}$) [31, 32], which constitute a two-legged qubit ladder [33], see Fig. 1**a**. By setting $\hbar = 1$, the system's Hamiltonian can be written as [34–36]

$$H = J_{\parallel} \sum_{j,s} (\hat{c}^{\dagger}_{j,s} \hat{c}_{j+1,s} + \text{H.c.}) + J_{\perp} \sum_{j} (\hat{c}^{\dagger}_{j,\uparrow} \hat{c}_{j,\downarrow} + \text{H.c.}) + \sum_{j,s} V_{j,s} \hat{c}^{\dagger}_{j,s} \hat{c}_{j,s}, \quad (1)$$

where $\hat{c}^{\dagger}$ ($\hat{c}$) is the hard-core bosonic creation (annihilation) operator with $(\hat{c}^{\dagger})^2 = \hat{c}^2 = 0$, and $[\hat{c}^{\dagger}_{i,s}, \hat{c}_{j,r}] = \delta_{ij}\delta_{sr}$. Here, $J_{\parallel}/2\pi \simeq 8$ MHz and $J_{\perp}/2\pi \simeq 7$ MHz denote the nearest-neighbour (NN) hopping between nearby qubits on the same leg and on the same rung, respectively, and $V_{j,s}$ is the tuneable on-site potential. Experimental details of our system are described in Supplementary Information.

With a dimensional reduction procedure [37], a 2D integer quantum Hall system can be mapped to a 1D model with a periodic parameter as a synthetic dimension. In this context, we experimentally simulate a 2D integer QHE associated with Chern insulator using 15 qubits on one leg of the ladder (i.e., qubits labelled by $Q_{1,\uparrow}$ to $Q_{15,\uparrow}$), where the on-site potential $V_{j,\uparrow}$ of each qubit is periodically modulated. This system can be described by the 1D Aubry-André-Harper (AAH) model [7, 8] with a tight-binding Hamiltonian

$$H_{\text{AAH}} = J_{\parallel} \sum_{j=1}^{14} (\hat{c}^{\dagger}_{j} \hat{c}_{j+1} + \text{H.c.}) + \Delta \sum_{j=1}^{15} \cos(2\pi b j + \phi) \hat{c}^{\dagger}_{j} \hat{c}_{j}, \quad (2)$$

where the second index $\uparrow$ is omitted. Here, b determines the modulation periodicity, and the modulation phase ϕ corresponds to the momentum in a synthetic dimension [37], see Fig. 1**b**. Note that there exists hopping between next-nearest neighbour (NNN) qubits $H' = J'_{\parallel} \sum_{j=1}^{13} (\hat{c}^{\dagger}_{j} \hat{c}_{j+2} + \text{H.c.})$ on the same leg with a strength $J'_{\parallel} \simeq 0.1 J_{\parallel}$, see Supplementary Information. This model is topologically equivalent to the lattice model of the 2D integer QHE, proposed by Hofstadter [38], where electrons hop within the 2D lattice, subjected to a perpendicular magnetic field with b being magnetic flux (normalised to the magnetic flux quantum) threading each unit cell. In our experiments, we fix $b = \frac{1}{3}$ and vary ϕ from 0 to 2π to obtain various instances of AAH models with potentials by tuning the qubits' frequencies as $\omega_j = \omega_0 + \Delta \sum_{j=1}^{15} \cos(2\pi b j + \phi)$, with a reference frequency $\omega_0/2\pi = 4.7$ GHz (Fig. 1**c**).

Band structure spectroscopy

Band structures play an essential role in characterising topological phases of matter and discovering novel classes of intriguing topological materials [3]. Here, we directly measure the topological band structure of the integer quantum Hall system along the synthetic dimension using a dynamic spectroscopic technique applied in refs. [34, 39, 40]. This method detects quantised eigenenergies of the quantum system from the Fourier transformation (FT) of the subsequent response of the system given local perturbations. The experimental sequence of pulses of the band structure spectroscopy are shown in Fig. 1**d**. With 15 qubits initialised at their idle points, we place one target qubit Q_j in the superposed state $|+_j\rangle = (|0_j\rangle + |1_j\rangle)/\sqrt{2}$, using a $Y_{\frac{\pi}{2}}$ pulse. Then, all qubits

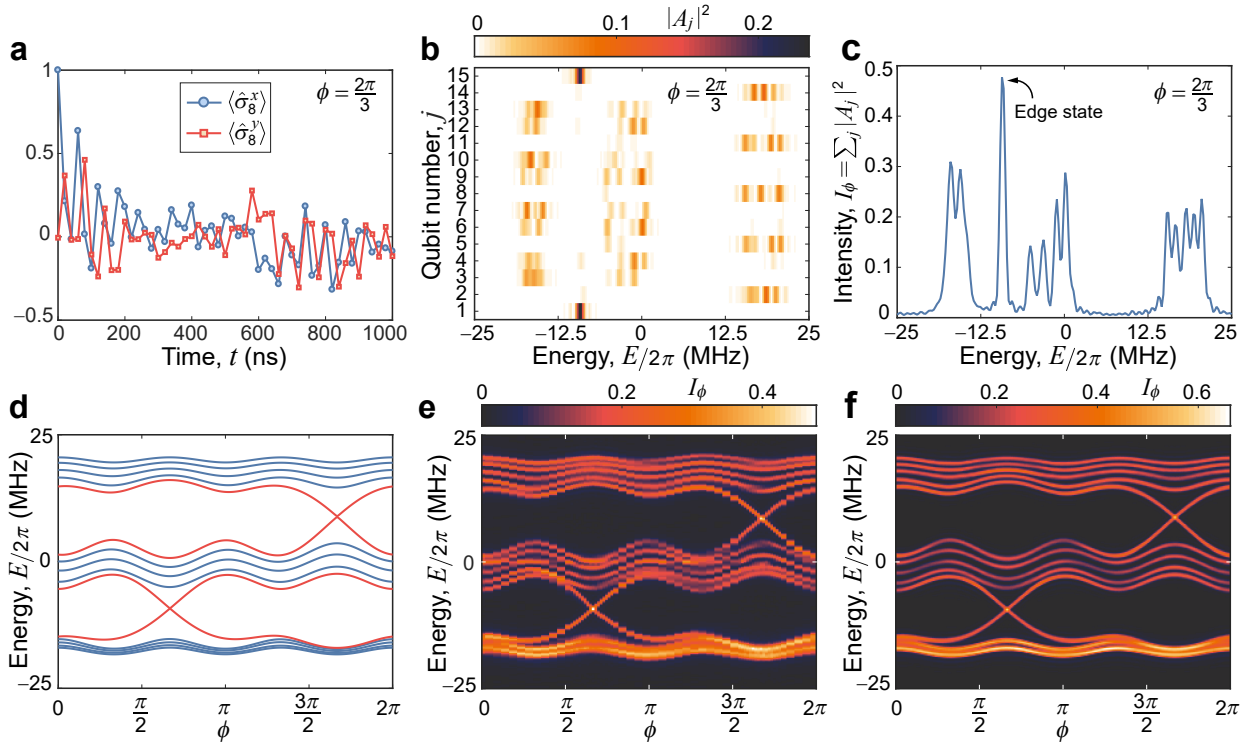


Fig. 2. **Band structure spectroscopy of the 2D Chern insulator with a synthetic dimension. a**, Typical data of $\langle\hat{\sigma}^x\rangle$ and $\langle\hat{\sigma}^y\rangle$ versus time t when choosing Q_8 as the target qubit for $b=\frac{1}{3}$, $\Delta/2\pi=12$ MHz and $\phi=\frac{2\pi}{3}$. **b**, Squared FT magnitudes $|A_j|^2$ of the response functions $\chi_j(t)\equiv\langle\hat{\sigma}_j^x(t)\rangle+i\langle\hat{\sigma}_j^y(t)\rangle$ for all fifteen qubits. Note that the edge states at the edge qubits: Q_1 and Q_{15}. **c**, Summation of the squared FT magnitudes $I_\phi\equiv\sum_j|A_j|^2$. **d**, Band structure of the 2D Chern insulator for $b=\frac{1}{3}$ and $\Delta=12$ MHz with 15 sites along the x-direction and periodic along the y direction. **e**, **f**, Experimentally measured data for I_ϕ (**e**) for different values of ϕ varied from 0 to 2π are compared with numerically calculated data of I_ϕ (**f**) obtained by numerically simulating the dynamics of the 15-qubit system without decoherence.

are detuned to their corresponding frequencies for the quench dynamics with a time t before the readout of the Q_j at its idle point in the $\hat{\sigma}^x$ and $\hat{\sigma}^y$ bases. For each ϕ, time evolutions of $\langle\hat{\sigma}_j^x\rangle$ and $\langle\hat{\sigma}_j^x\rangle$ are recorded when choosing a target qubit, e.g., Q_8 in Fig. 2**a**. Figure 2**b** shows the squared FT magnitude $|A_j|^2$ of the response function $\chi_j(t)\equiv\langle\hat{\sigma}_j^x(t)\rangle+i\langle\hat{\sigma}_j^y(t)\rangle$ for each qubit with $\phi=\frac{2\pi}{3}$ and $\Delta/2\pi=12$ MHz. With the summation of the squared FT magnitudes of all selected qubits $I_\phi\equiv\sum_j|A_j|^2$, the positions of its peaks clearly indicate the eigenenergies $E/2\pi$ of the system for each ϕ (Fig. 2**c**).

Simulating 2D Chern insulator with synthetic dimension

The topological nature of the 1D AAH model and the 2D integer QHE associated with Chern insulator can be identified from its band structure. When setting $\Delta/2\pi=12$ MHz, we plot in Fig. 2**d** the band structure of the 1D AAH model along ϕ with $N=15$ and open boundary conditions along x-direction. As ϕ evolves, the gapless edge states (red curves) appear in two gaps between three "bulk band" regimes (dense blue curves). We experimentally map out this band structure by measuring I_ϕ for $\phi\in[0,2\pi]$ (Fig. 2**e**), which also agrees well with the numerical result by simulating the system dynamics (Fig. 2**f**). Two gapless Dirac bands within two band gaps are clearly observed in Fig. 2**e**, and each gap is related to a quantised Hall conductance $\sigma=(e^2/h)\mathcal{C}$, with the integer $\mathcal{C}$ being determined by the Chern number [14].

Moreover, the topological edge states predicted in the band structure can be verified in real space by observing localisation of an edge excitation during its QWs on the 15-qubit chain [41]. After the system initialisation, we excite one qubit with a X_π pulse, tune all qubits to their corresponding frequencies and measure them at a time t after their free evolutions (Fig. 1**e**). For the topologically trivial case with $\Delta/2\pi=0$ MHz, the measured density distributions $P_j(t)$ of single-excitation QWs initialised at any position of the qubit chain show a light-cone-like propagation of information with boundary reflections [36]. When we set $b=\frac{1}{3}$ and $\Delta/2\pi=12$ MHz, the $P_j(t)$ for the excitation initialised at a boundary qubit (Q_1 or Q_{15}) exhibits localisation for $\phi=\frac{2\pi}{3}$, where the edge states appear in the middle of a band gap (Fig. 3**a1**, **a3**). This localised dynamical behaviour is due to the fact that the edge-excitation modes have a main overlap with the in-gap edge states which are topologically protected by the band gaps. This is also verified by the squared FT magnitudes $|A_1|^2$ and $|A_{15}|^2$ for edge qubits (Fig. 3**b1**, **b3**), which mainly contain information of the in-gap edge states. The

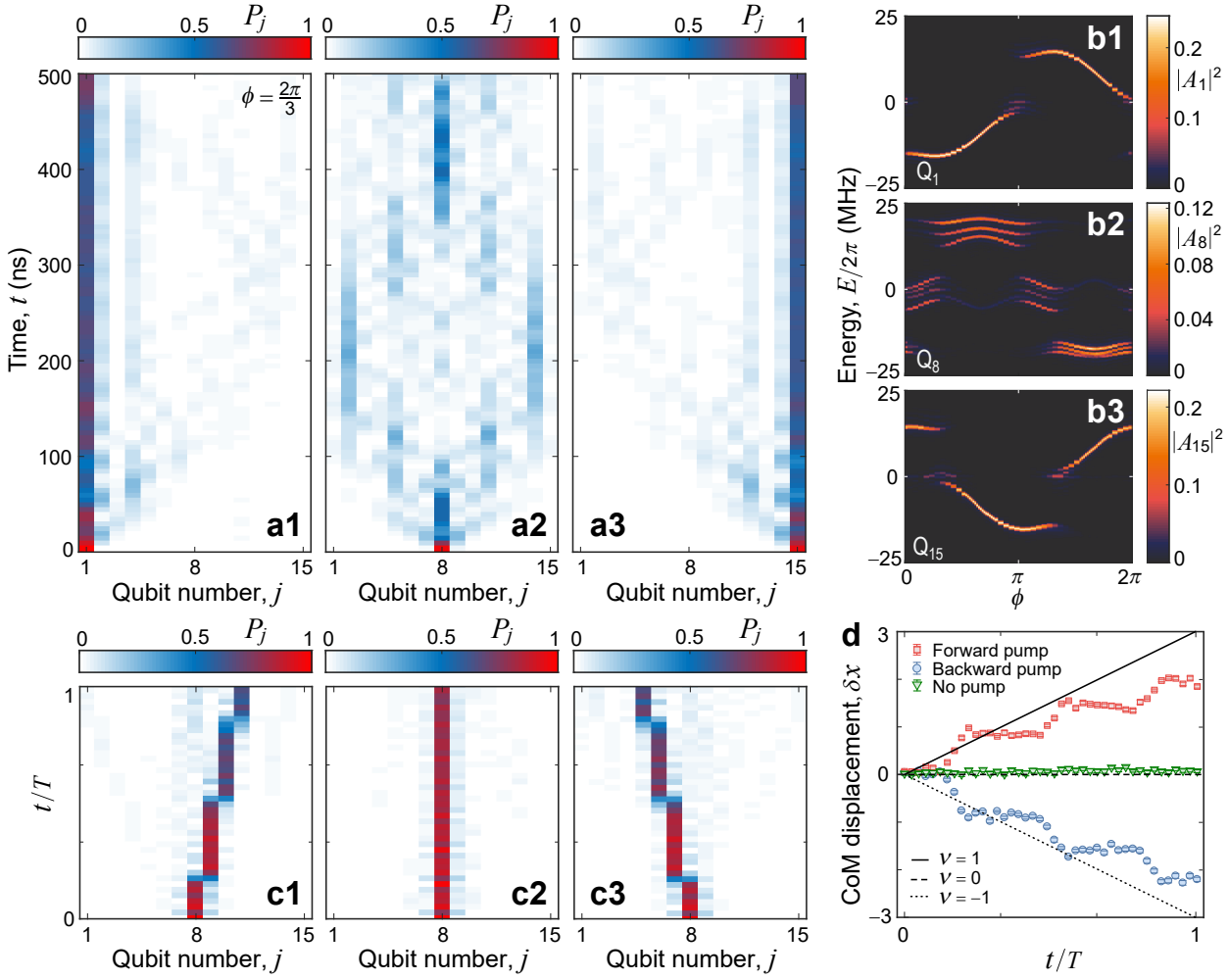


Fig. 3. **Dynamical signatures of topological edge states and the topological charge pump. a1–a3**, Time evolution of the excitation probability P_j with $b = \frac{1}{3}$, $\Delta/2\pi = 12$ MHz and $\phi = 2\pi/3$ after initially exciting the leftmost qubit Q_1 (**a1**), the central qubit Q_8 (**a2**), and the rightmost qubit Q_{15} (**a3**). **b1–b3**, Experimental data of the squared FT magnitudes $|A_1|^2$, $|A_8|^2$, and $|A_{15}|^2$, when choosing Q_1 (**b1**), Q_8 (**b2**), and Q_{15} (**b3**) as the target qubits. **c1–c3**, Time evolution of an excitation initially prepared at the central qubit Q_8 when it is forward pumped (**c1**), not pumped (**c2**) and backward pumped (**c3**), respectively, with $\Delta/2\pi = 36$ MHz for an initial $\phi_0 = 5\pi/3$. **d**, Displacement of the centre of mass (CoM) δx versus time t in one pumping cycle with period T for the cases in (**c1–c3**).

discontinuity of the FT signals for edge qubits results from the second and first band gaps, respectively, because the edge states localised at two boundaries have opposite propagation directions, like in the standard QHE. When a qubit away from either end, e.g. Q_8, is excited, we observe the propagation of the excitation in Fig. 3**a2** due to the absence of topological protection, and its FT signal $|A_8|^2$ merely shows partial information of the bulk band (Fig. 3**b2**). Thus, by directly measuring the band structure and observing dynamical localisation of edge excitations, our experiments demonstrate *the bulk-edge correspondence in the synthetic 2D Chern insulator*.

In addition, a topological charge pump, entailing the charge transport in a 1D time-varying potential driven in adiabatic cycles [17, 42], provides an alternative way to explore the 2D integer QHE. The charge transported in a pumping cycle is determined by the Chern number [43], which is defined over a 2D Brillouin zone with one spatial and one temporal dimensions. We experimentally simulate the charge pump by adiabatically varying ϕ in a 2π period starting from $\phi_0 = \frac{5\pi}{3}$ with $\Delta/2\pi = 36$ MHz. Figure 3**c1**, **c3** plot the evolutions of distributions $P_j(t)$ of an excitation initialised at the central qubit Q_8 for the forward and backward pumping schemes, respectively. In one pumping cycle, the excitation propagates through an integer number of unit cells, in this case three qubits, which is determined by the Chern number. Following Laughlin's argument [44, 45], the role of the threading magnetic flux is played by the adiabatic variation of ϕ, leading to the excitation's transport. The displacements of the centre of mass (CoM) δ_x are shown in Fig. 3**d**, of which the slight deviations from the Chern numbers ± 1 may result from the boundary reflection on the finite-size 1D qubit chain, fast pumps [46], and the small fraction of excitations for the higher bands. In

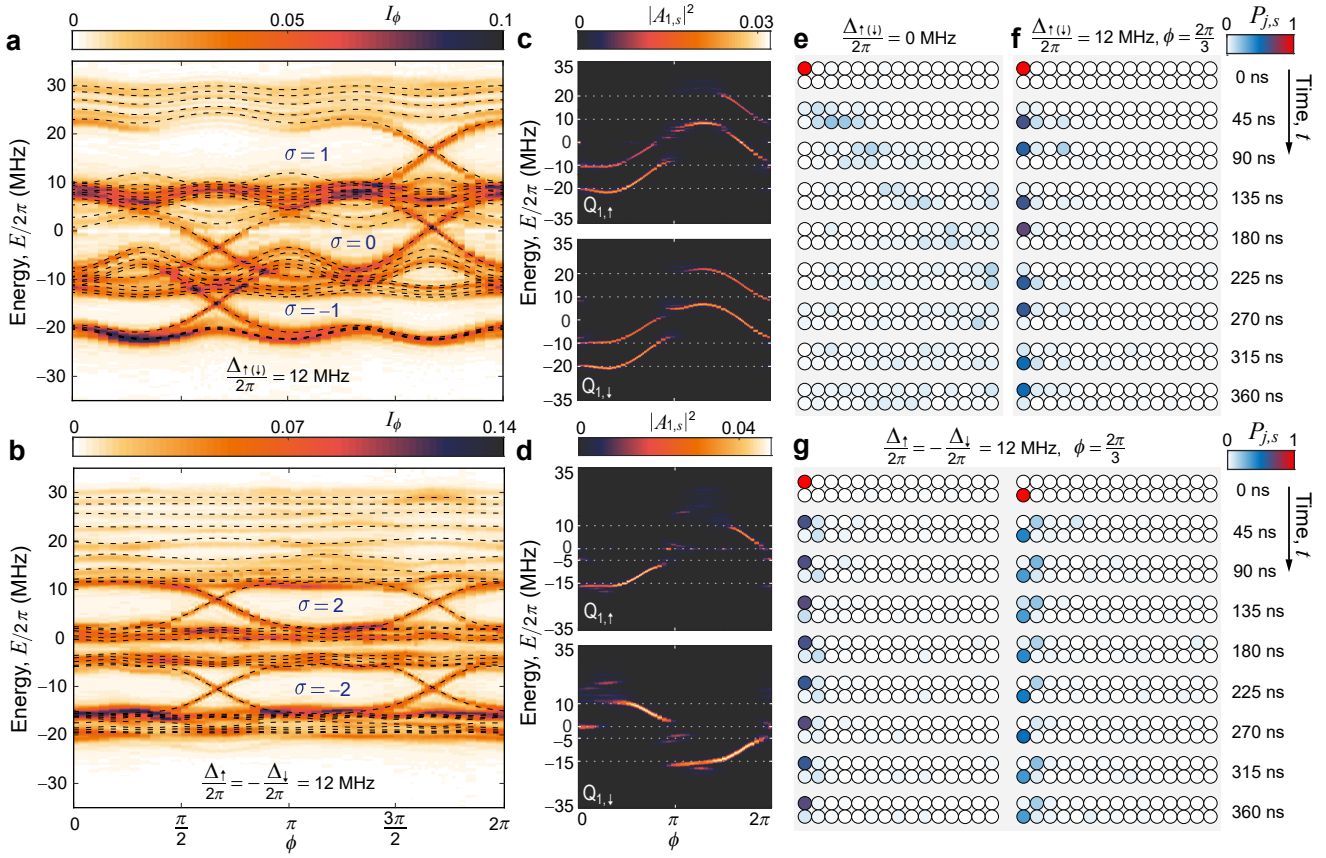


Fig. 4. **Quantum simulation of bilayer Chern insulators using all thirty qubits on a ladder-type quantum processor. a**,**b**, Experimentally measured I_ϕ with $b = \frac{1}{3}$ versus ϕ varied from 0 to 2π for two AAH chains with the same on-site potentials $\Delta_{\uparrow(\downarrow)}/2\pi = 12$ MHz (**a**) and opposite on-site potentials $\Delta_\uparrow/2\pi = -\Delta_\downarrow/2\pi = 12$ MHz (**b**), respectively, which are compared with the theoretical projected band structures (dashed curves). The Hall conductivity is defined as the summation of the Chern number $\mathcal{C}_n$ over the occupied bands: $\sigma = \sum_n \mathcal{C}_n$ by letting $e^2/h = 1$. **c**, **d**, Experimental data of the squared FT magnitudes $|A_{1,\uparrow}|^2$ and $|A_{1,\downarrow}|^2$ when choosing $Q_{1,\uparrow}$ and $Q_{1,\downarrow}$ as the target qubits for $\Delta_{\uparrow(\downarrow)}/2\pi = 12$ MHz (**c**) and $\Delta_\uparrow/2\pi = -\Delta_\downarrow/2\pi = 12$ MHz (**d**), respectively. **e**, **g**, Time evolutions of the excitation probability $P_{j,s}$, with $\phi = \frac{2\pi}{3}$, after initially exciting a corner qubit ($Q_{1,\uparrow}$ or $Q_{1,\downarrow}$) for $\Delta_{\uparrow(\downarrow)}/2\pi = 0$ MHz (**e**), $\Delta_{\uparrow(\downarrow)}/2\pi = 12$ MHz (**f**), and $\Delta_\uparrow/2\pi = -\Delta_\downarrow/2\pi = 12$ MHz (**g**), respectively. Animations of the time evolutions are available in Supplementary Video 1.

comparison, there exists no excitation transport when ϕ is not pumped (Fig. 3**c2**, **d**).

Simulating bilayer Chern insulators

Next, using all thirty qubits, we simulate two different bilayer Chern insulators. The Hamiltonian of the 30-qubit-ladder quantum processor is given in equation (1), where the on-site potentials on the qubits in two legs ($s \in \{\uparrow, \downarrow\}$) are modulated as

$$V_{j,s} = \Delta_s \cos(2\pi b j + \phi). \tag{3}$$

with $b = \frac{1}{3}$. For instances of two coupled AAH chains by varying ϕ with the same $\Delta_{\uparrow(\downarrow)}/2\pi = 12$ MHz and opposite $\Delta_\uparrow/2\pi = -\Delta_\downarrow/2\pi = 12$ MHz, we effectively simulate two different bilayer quantum systems, where the magnetic fluxes threading two layers are the same and have a difference of π, respectively. Using the above spectroscopic technique, we measure the band structures for these two cases (Figs. 4**a**, **b**), which agree well with the theoretical predictions (dashed curves) using experimental parameters in Supplementary Information.

For $\Delta_{\uparrow(\downarrow)}/2\pi = 12$ MHz with $J_\perp$ being comparable to $J_\parallel$, gapless edge states are experimentally observed (Fig. 4**a**), even when the Chern number for half filling is predicted to be zero (see Methods). This novel topological phase results from the existence of a pair of counter-propagating chiral edge states in the second gap (Fig. 4**c**), which are protected by the *inversion symmetry* and lead to a *zero* Hall conductivity $\sigma = 0$ [9]. When we excite a corner qubit (e.g., $Q_{1,\uparrow}$) and monitor the excitation's QWs for $\phi = \frac{2\pi}{3}$, the time-evolved distribution $P_{j,s}$ shows oscillations between two corner states localised at the same boundary rung of the qubit ladder (Fig. 4**f**). This dynamical behaviour can be further understood from the measured squared FT magnitudes $|A_{1,\uparrow}|^2$ and $|A_{1,\downarrow}|^2$ with respect to the corner qubits $Q_{1,\uparrow}$ and $Q_{1,\downarrow}$, respectively, which share information of the same edge states (Fig. 4**c**).

By modulating opposite on-site potential fields with $\Delta_\uparrow/2\pi = -\Delta_\downarrow/2\pi = 12$ MHz, we obtain a different band

structure (Fig. 4**b**) from the one with two layers having the same magnetic flux. In this case, the magnetic fluxes threading two layers have a difference of π, and the gapless edge states are characterised by higher Chern numbers (see Methods). The QWs of the excitation initialised at a corner qubit (e.g., $Q_{1,\uparrow}$ or $Q_{1,\downarrow}$) for $\phi = \frac{2\pi}{3}$ show dynamical localisation at the initial qubit (Fig. 4**g**), and the measured squared FT magnitudes of two corner qubits show information of different edge states in different gaps (Fig. 4**d**). Thus, this synthetic bilayer quantum system with two layers having a π-flux difference presents a Chern insulator with chiral edge states, identified by *higher* Chern numbers. Since high-Chern-number insulators without the formation of Landau levels have attracted increasing attentions [10–12], our work provides a new perspective for exploring these emergent topological phases. In comparison, for $\Delta_{\uparrow(\downarrow)}/2\pi = 0$, the QWs of the corner excitation first show linear propagation and then indicate thermalisation on the qubit ladder as a non-integrable system [35, 47].

Conclusions and outlook

In summary, we simulate the 2D and bilayer Chern insulators with synthetic dimensions on a programable 30-qubit-ladder superconducting processor. By measuring the band structures and monitoring dynamical localisation of edge excitations, we implement the bulk-edge correspondence in the 2D Chern insulator. In addition, we synthesise two different bilayer Chern insulators with two layers having the same magnetic flux and a π-flux difference, respectively, and simulate distinct and novel topological phases. Our experiments, using a relatively large number of superconducting qubits with long coherence times and accurate readouts, show the future potential of using superconducting simulating platforms for investigating intriguing topological quantum phases and quantum many-body physics.

Methods

System Hamiltonian

Our superconducting quantum processor can be described as a Bose-Hubbard ladder with a Hamiltonian ($\hbar = 1$) [34, 35]

$$H_{\rm BH} = J_{\parallel}\sum_{j,s}(\hat{a}^{\dagger}_{j,s}\hat{a}_{j+1,s} + \text{H.c.}) + \sum_{j,s}\frac{\eta_{j,s}}{2}\hat{n}_{j,s}(\hat{n}_{j,s}-1) + J_{\perp}\sum_{j}(\hat{a}^{\dagger}_{j,\uparrow}\hat{a}_{j,\downarrow} + \text{H.c.}) + \sum_{j,s}V_{j,s}\hat{n}_{j,s}, \quad (4)$$

where $\hat{a}^{\dagger}$ ($\hat{a}$) is the bosonic creation (annihilation) operator, and $\hat{n} \equiv \hat{a}^{\dagger}\hat{a}$ is the number operator. Here, $J_{\parallel}/2\pi \simeq 8$ MHz and $J_{\perp}/2\pi \simeq 7$ MHz denote the nearest-neighbour (NN) hopping between nearby qubits on the same leg and on the same rung, respectively. Also, η is the on-site nonlinear interaction, and $V_{j,s}$ is the tuneable on-site potential.

Our device is designed to fulfil the hard-core limit $|\eta/J| \gg 1$, and thus, the highly occupied states of transmon qubits are blockaded, which represents fermionisation of strongly interacting bosons [36]. The system's Hamiltonian can then be simplified as

$$H = J_{\parallel}\sum_{j,s}(\hat{c}^{\dagger}_{j,s}\hat{c}_{j+1,s} + \text{H.c.}) + \sum_{j,s}V_{j,s}\hat{c}^{\dagger}_{j,s}\hat{c}_{j,s} + J_{\perp}\sum_{j}(\hat{c}^{\dagger}_{j,\uparrow}\hat{c}_{j,\downarrow} + \text{H.c.}), \quad (5)$$

where $\hat{c}^{\dagger}$ ($\hat{c}$) is the hard-core bosonic creation (annihilation) operator with $(\hat{c}^{\dagger})^2 = \hat{c}^2 = 0$, and $[\hat{c}^{\dagger}_{j,s}, \hat{c}_{i,r}] = \delta_{ji}\delta_{sr}$.

Note that in addition to the hopping between nearest-neighbour (NN) qubits, there also exist the hopping between next-nearest neighbour (NNN) qubits on different legs:

$$J_{\times}\sum_{j}(\hat{c}^{\dagger}_{j,\uparrow}\hat{c}_{j+1,\downarrow} + \hat{c}^{\dagger}_{j,\downarrow}\hat{c}_{j+1,\uparrow} + \text{H.c.}), \quad (6)$$

and the hopping between third-nearest-neighbour (TNN) qubits on the same leg:

$$J'_{\parallel}\sum_{j,s}(\hat{c}^{\dagger}_{j,s}\hat{c}_{j+2,s} + \text{H.c.}). \quad (7)$$

Mapping the 2D quantum Hall model to various instances of Aubry-André-Harper chains

An electron moving in a 2D lattice with a perpendicular magnetic field b is described by the integer quantum Hall model,

$$H_{\rm IQH} = t_x\sum_{j=1}^{N-1}\sum_{m=1}^{M}(\hat{c}^{\dagger}_{j,m}\hat{c}_{j+1,m} + \text{H.c.}) + t_y\sum_{j=1}^{N}\sum_{m=1}^{M}(\hat{c}^{\dagger}_{j,m}\hat{c}_{j,m+1}e^{i2\pi bj} + \text{H.c.}), \quad (8)$$

where t_x and t_y are hopping strengths along the x and y-axes, respectively. We consider a periodic boundary condition in the y-direction and introduce the Fourier transformation (FT):

$$\hat{c}_{j,k_y} = \sum_{m=1}^{M}e^{-ik_y m}\hat{c}_{j,m}, \qquad \hat{c}^{\dagger}_{j,k_y} = \sum_{m=1}^{M}e^{ik_y m}\hat{c}^{\dagger}_{j,m}. \quad (9)$$

Then, the Hamiltonian transforms to $H_{\rm IQH} = \sum_{k_y}H_{k_y}$, with k_y being the quasi-momentum in the y-direction, where

$$H_{k_y} = t_x\sum_{j}^{N-1}(\hat{c}^{\dagger}_{j,k_y}\hat{c}_{j+1,k_y} + \text{H.c.}) + 2t_y\sum_{n}^{N}\cos(2\pi bj + k_y)\hat{c}^{\dagger}_{j,k_y}\hat{c}_{j,k_y}. \quad (10)$$

By replacing t_x, $2t_y$, and q with J, Δ, and ϕ, we obtain the 1D Aubry-André-Harper (AAH) model

$$H_{\rm AAH} = J\sum_{j}^{N-1}(\hat{c}^{\dagger}_{j}\hat{c}_{j+1} + \text{H.c.}) + \Delta\sum_{j}^{N}\cos(2\pi bj + \phi)\hat{c}^{\dagger}_{j}\hat{c}_{j}, \quad (11)$$

where the second index has been omitted in the 15-qubit experiment.

Since we simulated a 1D tight-binding fermionic Hamiltonian (11) in our experiments, to investigate the behaviour of one excitation (a hard-core boson) effectively captures the topological property of the system. Furthermore, in the case when we only excite one qubit, the interaction term in equation (4) is zero, and the behaviour of the quantum system we simulated is not affected by the statistics of the particle (fermionic or bosonic). Since our device is designed to fulfil the hard-core limit $|\eta/J| \simeq 25 \gg 1$, the highly occupied states of transmon qubits are blockaded, which represents fermionisation of strongly interacting bosons [36]. Thus, the dynamical behaviour of a multiple-excitation system in the 15-qubit-chain experiment is similar as a 1D fermionic system, as demonstrated in ref. [36].

Band structure spectroscopy and effect of decoherence

After initialising the selected qubits at their idle points, we prepare one target qubit $Q_{j,s}$ in the superposed state $|+_{j,s}\rangle = (|0_{j,s}\rangle + |1_{j,s}\rangle)/\sqrt{2}$, using a $Y_{\frac{\pi}{2}}$ pulse. Then, all qubits are tuned to their corresponding frequencies for the quench dynamics, and at a time t, we measure the $Q_{j,s}$ at its idle point in the $\hat{\sigma}^x$ and $\hat{\sigma}^y$ bases. For each ϕ, time evolutions of $\langle\hat{\sigma}^x_{j,s}(t)\rangle$ and $\langle\hat{\sigma}^y_{j,s}(t)\rangle$ are monitored. Then, we calculate the squared Fourier transformation (FT) magnitude $|A_{j,s}|^2$ of the response function [34]

$$\chi_{j,s}(t) \equiv \langle\hat{\sigma}^x_{j,s}(t)\rangle + i\langle\hat{\sigma}^y_{j,s}(t)\rangle. \tag{12}$$

With the summation of the squared FT magnitudes of all selected qubits $I_\phi \equiv \sum_{j,s}|A_{j,s}|^2$, the positions of its peaks clearly indicate the eigenenergies $\{E_n\}$ of the system for each ϕ.

Given $|\Psi_{j,s}(0)\rangle = \sum_n c_n^{(j,s)}|\psi_n\rangle$, with $H|\psi_n\rangle = E_n|\psi_n\rangle$ and $c_n^{(j,s)} \equiv \langle\psi_n|\Psi_{j,s}(0)\rangle$, and the evolution of the state can be obtained by solving the Schrödinger equation as

$$|\Psi_{j,s}(t)\rangle = e^{-iHt}|\Psi_{j,s}(0)\rangle = \sum_n c_n^{(j,s)}e^{-itE_n}|\psi_n\rangle. \tag{13}$$

We obtain the response function of the system after the initial perturbation as

$$\chi_{j,s}(t) \sim 2\langle\Psi_{j,s}(0)|\Psi_{j,s}(t)\rangle - 1 = 2\sum_n |c_n^{(j,s)}|^2 e^{-itE_n} - 1, \tag{14}$$

and the FT of the response function is calculated as

$$\begin{aligned}\tilde{\chi}_{j,s}(\omega) &\sim \frac{1}{2\pi}\int d\omega \left[2\sum_n |c_n^{(j,s)}|^2 e^{-it(E_n-\omega)} - e^{i\omega t}\right] \\ &= 2\sum_n |c_n^{(j,s)}|^2\delta(\omega - E_n) - \delta(\omega),\end{aligned} \tag{15}$$

where the eigenenergies $\{E_n\}$ are indicated by the peaks of the FT signals.

Furthermore, when considering decoherence with a decaying rate γ in a form

$$\begin{aligned}\chi_{j,s}(t) &\sim 2\langle\Psi_{j,s}(0)|\Psi_{j,s}(t)\rangle - 1 \\ &= \left[2\sum_n |c_n^{(j,s)}|^2\delta(\omega - E_n) - \delta(\omega)\right] e^{-\gamma t},\end{aligned} \tag{16}$$

the FT of the response function is calculated as

$$\begin{aligned}\tilde{\chi}_{j,s}(\omega) &\sim \frac{1}{2\pi}\int d\omega \sum_n |c_n^{(j,s)}|^2 e^{-it(E_n-\omega)} \\ &= \sum_n |c_n^{(j,s)}|^2 \frac{4\gamma}{\gamma^2 + (\omega - E_n)^2} - \frac{2\gamma}{\gamma^2 + \omega^2},\end{aligned} \tag{17}$$

which indicates that the presence of decoherence increases the width of the peaks of the FT signals, and the locations of the peaks can still indicate the values of the eigenenergies.

There also exists the unwanted zero frequency signal of the FT. In our experiments, to eliminate the unwanted zero frequency signal of the FT we calculate the FT of oscillations of the response function $\delta\chi(t) \equiv \chi(t) - \overline{\chi(t)}$, i.e., the response function minus the its average over the time interval.

Avoiding rung-pair excitations in strongly interacting Bose-Hubbard ladders

In the 30-qubit-ladder experiment, we excited either one corner qubit or a bulk qubit and monitored the quantum walks of the excitation, to study the topologically protected edge states of the bilayer quantum Hall systems. Localisation of the excitation initialised at a corner qubit and the propagation of the excitation initialised at the bulk qubit indicate the existence of a topological edge state protected by the topology of the bulk structure.

However, we do not consider to excite two corner qubits at the same edge simultaneously, because it has been experimentally and theoretically shown in refs. [35, 48] that the dynamics of single- and double-excitation states have very distinct behaviours. Specifically, in the hard-core limit, there exists rung-pair localisation at the edges even for the topologically trivial case without the modulation of the on-site potentials, $\Delta_\uparrow/2\pi = \Delta_\downarrow/2\pi = 12$ MHz. In the centre-of-mass frame, the two-particle system can be mapped into an effective single-particle Hamiltonian, and there exists a zero-energy flat band in the hard-core limit, which is the origin of the localisation [48]. Therefore, in the 30-qubit-ladder experiment, we avoid exciting two qubits on the same rung simultaneously, when investigating the topologically-protected edge states.

Quantum charge pumping

In addition to the study of 2D topological systems, topological charge pumping provides an alternative way to explore the quantised transport with topological protection in a dynamical 1D system. The concept of topological charge pumping was first proposed by D. J. Thouless [17], and recognised a topological quantisation of charge transport in a 1D time-varying

potential driven in adiabatic cycles. The charge transported in a pumping cycle is determined by the Chern number [14], which is defined over a 2D Brillouin zone with one spatial dimension and one temporal dimension.

We experimentally simulate the quantum charge pump by adiabatically varying ϕ in a 2π period starting from $\phi_0 = \frac{5\pi}{3}$ with $\Delta/2\pi = 36$ MHz. After initialising 15 qubits in the state $|0\rangle^{\otimes 15}$ at their idle frequencies, we prepared the central qubit, $Q_{8,\uparrow}$, in the $|1\rangle$ state. Then, we set the frequencies of qubits as $\omega_j(\phi) = \omega_0 + \Delta \sum_{j=1}^{15} \cos(2\pi bj + \phi)$, with $\Delta/2\pi = 36$ MHz and an initial phase $\phi_0 = \frac{5\pi}{3}$. In this case, the single-excitation initial state has the minimum energy, and with a high value of Δ, the initial excitation stabilises at $Q_{8,\uparrow}$. The frequencies for all qubits are calibrated using the frequency calibration procedure as shown in Supplementary Information. Then, by modulating the frequencies of all 15 qubits simultaneously, we slowly vary ϕ from ϕ_0 to $\phi_0 \pm 7.7$ rad in 500 ns with a relatively slow speed $\sim 4.9\pi/\mu$s for the backward and forward pumping schemes, respectively. For the case of no pump, ϕ is fixed at ϕ_0 during the time evolution.

In our experiments, we measured the $|1\rangle$-state occupation probability of each qubit at its idle point in the $\hat{\sigma}^z$ basis for each evolution time t. To reduce the effect of the stochastic fluctuations, we maintained a fixed sample of 3,000 single-shot readouts and repeated the measurement procedure 8 times (16 times for the no pump case) for estimating the mean values and standard deviations at each evolution time t. We obtained the average displacements of the centre of mass (CoM) as

$$\delta x(t) = \sum_{j=1}^{15} P_{j,\uparrow}(t)(j-8)/3, \tag{18}$$

where $P_j(t)$ is the $|1\rangle$-state occupation probability of the $Q_{j,\uparrow}$. Note that the CoM is divided by 3, because we set $b = \frac{1}{3}$ and there are 3 qubits in one unit cell. The experimental results can be found in Fig. 3 in the main text.

Characterisation of bilayer Chern insulators

The Hamiltonian of the 30-qubit ladder reads

$$\begin{aligned} H = &\sum_{j,s} (J_\parallel \hat{c}^\dagger_{j,s}\hat{c}_{j+1,s} + J'_\parallel \hat{c}^\dagger_{j,s}\hat{c}_{j+2,s} + \text{H.c.}) \\ &+ J_\perp \sum_j (\hat{c}^\dagger_{j,\uparrow}\hat{c}_{j,\downarrow} + \text{H.c.}) \\ &+ J_\times \sum_j (\hat{c}^\dagger_{j,\uparrow}\hat{c}_{j+1,\downarrow} + \hat{c}^\dagger_{j,\downarrow}\hat{c}_{j+1,\uparrow} + \text{H.c.}) \\ &+ \sum_{j,s} \Delta_s \cos(2\pi b_s j + \phi)\, \hat{c}^\dagger_{j,s}\hat{c}_{j,s}, \end{aligned} \tag{19}$$

where $s \in \{\uparrow, \downarrow\}$, and $b = \frac{1}{3}$ determines the modulation periodicity. The typical hopping strengths for our sample are $J_\parallel/2\pi = 8$ MHz, $J_\perp/2\pi = 7$ MHz, $J'_\parallel \simeq 0.1J_\parallel$, and $J_\times \simeq 0.2J_\parallel$. The AAH ladder can be mapped into two coupled Hofstadter lattices, subjected to the same effective magnetic fields for each layer.

We now proceed to discuss the topological properties in two cases, i.e.,

$$\Delta_\uparrow = \Delta_\downarrow = \Delta, \text{ and } \Delta_\uparrow = -\Delta_\downarrow = \Delta.$$

They correspond to the study of two types of bilayer quantum systems with two layers having the same magnetic flux and a π-flux difference, respectively. In our experiments, we set $\Delta/2\pi = 12$ MHz.

Two qubit chains with the same periodically modulated on-site potentials. For $\Delta_\uparrow = \Delta_\downarrow = \Delta$, two identical AAH chains are coupled to form an AAH ladder. In Extended Data Fig. 1, we plot the band structures for different inter-chain hopping strengths $J_\perp$. Extended Data Figure 1 shows the energy spectra of different topological phase regimes, showing that topological phase transitions occur as $J_\perp$ varies.

We can identify the topologically nontrivial and trivial bands by using the Chern number of each band [14], which is defined as

$$\mathcal{C}_n = \frac{1}{2\pi}\int_0^{2\pi} dk \int_0^{2\pi} d\phi \, \left[\partial_k \mathcal{A}^n_\phi - \partial_\phi \mathcal{A}^n_k\right]. \tag{20}$$

The nth band Berry connection $\mathcal{A}^n$ is written as

$$\mathcal{A}^n_\gamma = i\langle \varphi_n(k,\phi)|\partial_\gamma|\varphi_n(k,\phi)\rangle, \tag{21}$$

where $|\varphi_n(k,\phi)\rangle$ is the nth band's wavefunction, and $\gamma = k, \phi$. Then, the Hall conductivity reads $\sigma = \sum_n \mathcal{C}_n$, with n being summed over the occupied bands.

When the inter-chain hopping strength $J_\perp$ is much smaller (Extended Data Fig. 1**a**) or much larger (Extended Data Fig. 1**c**) than the intra-chain hoping strength $J_\parallel$, the topological boundary states are well characterised by the Chern number. However, when $J_\perp$ is comparable to $J_\parallel$, topological edge states with zero Hall conductivity appear (Extended Data Fig. 1**b**) for the half filling.

The zero Hall conductivity results from the contribution of a pair of counter-propagating chiral edge states. This novel topological phase was also studied in a dimerised Hofstadter model [9] and has never been experimentally observed before. Extended Data Figure 2 shows the density distribution of a mid-gap state for the half filling, where the in-gap state occupies the end sites of both chains.

The topological edges with zero Chern number (i.e., zero Hall conductivity) is protected by the inversion symmetry. After Fourier transforming equation (19), we have the following momentum-space Hamiltonian

$$H(k)=\sum_{\mathbf{k}}\Phi_{\mathbf{k}}^{\dagger}\begin{pmatrix}\Delta\cos(\frac{2\pi}{3}+\phi) & J_{\parallel}+J'_{\parallel}e^{-ik} & J_{\parallel}e^{-ik}+J'_{\parallel} & J_{\perp} & J_{\times} & J_{\times}e^{-ik}\\ J_{\parallel}+J'_{\parallel}e^{ik} & \Delta\cos(\frac{4\pi}{3}+\phi) & J_{\parallel}+J'_{\parallel}e^{-ik} & J_{\times} & J_{\perp} & J_{\times}\\ J_{\parallel}e^{ik}+J'_{\parallel} & J_{\parallel}+J'_{\parallel}e^{ik} & \Delta\cos(\phi) & J_{\times}e^{ik} & J_{\times} & J_{\perp}\\ J_{\perp} & J_{\times} & J_{\times}e^{-ik} & \Delta\cos(\frac{2\pi}{3}+\phi) & J_{\parallel}+J'_{\parallel}e^{-ik} & J_{\parallel}e^{-ik}+J'_{\parallel}\\ J_{\times} & J_{\perp} & J_{\times} & J_{\parallel}+J'_{\parallel}e^{ik} & \Delta\cos(\frac{4\pi}{3}+\phi) & J_{\parallel}+J'_{\parallel}e^{-ik}\\ J_{\times}e^{ik} & J_{\times} & J_{\perp} & J_{\parallel}e^{ik}+J'_{\parallel} & J_{\parallel}+J'_{\parallel}e^{ik} & \Delta\cos(\phi)\end{pmatrix}\Phi_{\mathbf{k}}, \tag{22}$$

where $\Phi_{\mathbf{k}}=(\hat{c}_{k,1,\uparrow},\ \hat{c}_{k,2,\uparrow},\ \hat{c}_{k,3,\uparrow},\ \hat{c}_{k,1,\downarrow},\ \hat{c}_{k,2,\downarrow},\ \hat{c}_{k,3,\downarrow})^{T}$, with $\hat{c}_{k,l,s}$ ($l=1,2,3$ and $s\in\{\uparrow,\downarrow\}$) being the annihilation operator of a hardcore boson at momentum k, sublattice l, and pesudospin s.

The Hamiltonian $H(k)$ in equation (22) has the inversion symmetry

$$\hat{\mathcal{P}}H(k)\hat{\mathcal{P}}^{-1}=H(-k), \tag{23}$$

for $\phi=\frac{2\pi}{3}$ and $\phi=\frac{5\pi}{3}$, where the inversion symmetry operator $\hat{\mathcal{P}}$ is

$$\hat{\mathcal{P}}=\begin{pmatrix}0&0&0&0&0&1\\0&0&0&0&1&0\\0&0&0&1&0&0\\0&0&1&0&0&0\\0&1&0&0&0&0\\1&0&0&0&0&0\end{pmatrix}. \tag{24}$$

Then, we define an integer invariant $\mathcal{N}$ to characterize this novel topological phase, which is expressed as [9]

$$\mathcal{N}\equiv|N_1-N_2|, \tag{25}$$

where N_1 and N_2 are the number of negative parities (by applying the inversion symmetry operator to eigenstates) at the high symmetry points $k=0$ and $k=\pi$, respectively.

Extended Data Figure 3 shows the Bloch band structures for $\phi=\frac{2\pi}{3}$ and $\phi=\frac{5\pi}{3}$, respectively, and the topological invariant $\mathcal{N}$ at each band gap is indicated. For $\phi=\frac{2\pi}{3}$, we find $\mathcal{N}=1$ for $\frac{1}{4}$-filling and half-filling, indicating a pair of edge states pinned at $\phi=\frac{2\pi}{3}$. For $\phi=\frac{5\pi}{3}$, we have $\mathcal{N}=1$ for $\frac{3}{4}$-filling and half-filling, indicating a pair of edge states pined at $\phi=\frac{5\pi}{3}$. Therefore, two pairs of edge states appear at half-filling, which propagate in opposite directions at each edge.

Two qubit chains with opposite periodically modulated on-site potentials. For $\Delta_{\uparrow}=-\Delta_{\downarrow}=\Delta$, the AAH ladder shows two typical topological band structures, as shown in Extended Data Fig. 4. This bilayer structure, with two layers having a π-flux difference, shows different topological features from the bilayer structure with two layers having the same magnetic flux. Furthermore, the in-gap states mainly occupy the end site of one of the chains, as shown in Extended Data Fig. 5. Thus, this synthetic bilayer quantum system, with two layers having a π-flux difference, presents an integer quantum Hall effect with chiral edge states, identified by higher Chern numbers.

Data availability

The data presented in the figures and that support the other findings of this study are available from the corresponding author on reasonable request.

Code availability

The codes are available upon reasonable request from the corresponding author.

acknowledgments We thank Hongming Weng for stimulating discussions. This research was supported by the NSFC (Grants No. T2121001, No. 11934018, No. 11904393, No. 92065114, No. 12174207), the CAS Strategic Priority Research Program (Grant No. XDB28000000, No. YJKYYQ20200041), the Beijing Natural Science Foundation (Grant No. Z200009), the State Key Development Program for Basic Research of China (Grant No. 2017YFA0304300), the Key-Area Research and Development Program of Guangdong Province China (Grant No. 2020B0303030001), the NTT Research, the ARO (Grant No. W911NF-18-1-0358), the JST (via the Q-LEAP, and the Moonshot R&D Grant No. JPMJMS2061), the JSPS (via the Postdoctoral Fellowship Grant No. P19326, the KAKENHI Grants No. JP19F19326, No. JP20H00134), the AOARD (Grant No. FA2386-20-1-4069), and the FQXi (Grant No. FQXi-IAF19-06).

Author contributions Y.-R.Z., T.L., K.X., F.N., and H.F. conceived the research. Y.-R.Z., T.L., Z.-C.X., K.H., K.X., F.N., and H.F. designed the experiment. Z.-C.X. designed and fabricated the device. K.H., C.-L.D and K.X. performed the experiment. K.H., Y.-R.Z., and Y.-H.S. performed numerical simulations. K.H., Y.-R.Z., and Z.-C.X. analysed experimental results. T.L., Y.-R.Z., F.N., and H.F. performed theoretical explanations. G.X and H.Y. provide the Josephson Parametric Amplifiers. All authors contributed to the experimental setup, discussions of the results, and the development of the manuscript. F.N. and H.F. supervised the whole project.

Competing interests The authors declare no competing interests.

* These authors contributed equally to this work.

† kaixu@iphy.ac.cn
‡ fnori@riken.jp
§ hfan@iphy.ac.cn

[1] M. Z. Hasan and C. L. Kane, Colloquium: Topological insulators, Rev. Mod. Phys. **82**, 3045 (2010).
[2] X.-L. Qi and S.-C. Zhang, Topological insulators and superconductors, Rev. Mod. Phys. **83**, 1057 (2011).
[3] A. Bansil, H. Lin, and T. Das, Colloquium: Topological band theory, Rev. Mod. Phys. **88**, 021004 (2016).
[4] I. M. Georgescu, S. Ashhab, and F. Nori, Quantum simulation, Rev. Mod. Phys. **86**, 153 (2014).
[5] L. Yuan, Q. Lin, M. Xiao, and S. Fan, Synthetic dimension in photonics, Optica **5**, 1396 (2018).
[6] T. Ozawa and H. M. Price, Topological quantum matter in synthetic dimensions, Nat. Rev. Phys. **1**, 349 (2019).
[7] P. G. Harper, The general motion of conduction electrons in a uniform magnetic field, with application to the diamagnetism of metals, Proc. Phys. Soc. A **68**, 879 (1955).
[8] S. Aubry and G. André, Analyticity breaking and Anderson localization in incommensurate lattices, Ann. Israel Phys. Soc **3**, 18 (1980).
[9] A. Lau, C. Ortix, and J. van den Brink, Topological edge states with zero Hall conductivity in a dimerized Hofstadter model, Phys. Rev. Lett. **115**, 216805 (2015).
[10] J. Ge, Y. Liu, J. Li, H. Li, T. Luo, Y. Wu, Y. Xu, and J. Wang, High-Chern-number and high-temperature quantum Hall effect without Landau levels, Natl. Sci. Rev. **7**, 1280 (2020).
[11] G. Chen, A. L. Sharpe, E. J. Fox, Y.-H. Zhang, S. Wang, L. Jiang, B. Lyu, H. Li, K. Watanabe, T. Taniguchi, Z. Shi, T. Senthil, D. Goldhaber-Gordon, Y. Zhang, and F. Wang, Tunable correlated Chern insulator and ferromagnetism in a moiré superlattice, Nature **579**, 56 (2020).
[12] Y.-F. Zhao, R. Zhang, R. Mei, L.-J. Zhou, H. Yi, Y.-Q. Zhang, J. Yu, R. Xiao, K. Wang, N. Samarth, M. H. W. Chan, C.-X. Liu, and C.-Z. Chang, Tuning the Chern number in quantum anomalous Hall insulators, Nature **588**, 419 (2020).
[13] K. von Klitzing, G. Dorda, and M. Pepper, New method for high-accuracy determination of the fine-structure constant based on quantized Hall resistance, Phys. Rev. Lett. **45**, 494 (1980).
[14] D. J. Thouless, M. Kohmoto, M. P. Nightingale, and M. den Nijs, Quantized Hall conductance in a two-dimensional periodic potential, Phys. Rev. Lett. **49**, 405 (1982).
[15] A. Dutt, Q. Lin, L. Yuan, M. Minkov, M. Xiao, and S. Fan, A single photonic cavity with two independent physical synthetic dimensions, Science **367**, 59 (2020).
[16] C. Leefmans, A. Dutt, J. Williams, L. Yuan, M. Parto, F. Nori, S. Fan, and A. Marandi, Topological dissipation in a time-multiplexed photonic resonator network, Nat. Phys. **18**, 442 (2022).
[17] D. J. Thouless, Quantization of particle transport, Phys. Rev. B **27**, 6083 (1983).
[18] M. Lohse, C. Schweizer, H. M. Price, O. Zilberberg, and I. Bloch, Exploring 4D quantum Hall physics with a 2D topological charge pump, Nature **553**, 55 (2018).
[19] O. Zilberberg, S. Huang, J. Guglielmon, M. Wang, K. P. Chen, Y. E. Kraus, and M. C. Rechtsman, Photonic topological boundary pumping as a probe of 4D quantum Hall physics, Nature **553**, 59 (2018).
[20] G. Jotzu, M. Messer, R. Desbuquois, M. Lebrat, T. Uehlinger, D. Greif, and T. Esslinger, Experimental realization of the topological Haldane model with ultracold fermions, Nature **515**, 237 (2014).
[21] M. Aidelsburger, M. Lohse, C. Schweizer, M. Atala, J. T. Barreiro, S. Nascimbène, N. R. Cooper, I. Bloch, and N. Goldman, Measuring the Chern number of Hofstadter bands with ultracold bosonic atoms, Nat. Phys. **11**, 162 (2015).
[22] T. Chalopin, T. Satoor, A. Evrard, V. Makhalov, J. Dalibard, R. Lopes, and S. Nascimbene, Probing chiral edge dynamics and bulk topology of a synthetic Hall system, Nat. Phys. **16**, 1017 (2020).
[23] Z. Wang, Y. Chong, J. D. Joannopoulos, and M. Soljačić, Observation of unidirectional backscattering-immune topological electromagnetic states, Nature **461**, 772 (2009).
[24] M. Hafezi, S. Mittal, J. Fan, A. Migdall, and J. M. Taylor, Imaging topological edge states in silicon photonics, Nat. Photon. **7**, 1001 (2013).
[25] A. B. Khanikaev and G. Shvets, Two-dimensional topological photonics, Nat. Photon. **11**, 763 (2017).
[26] J. Ningyuan, C. Owens, A. Sommer, D. Schuster, and J. Simon, Time- and site-resolved dynamics in a topological circuit, Phys. Rev. X **5**, 021031 (2015).
[27] S. Klembt, T. H. Harder, O. A. Egorov, K. Winkler, R. Ge, M. A. Bandres, M. Emmerling, L. Worschech, T. C. H. Liew, M. Segev, C. Schneider, and S. Höfling, Exciton-polariton topological insulator, Nature **562**, 552 (2018).
[28] K. J. Satzinger, Y.-J. Liu, A. Smith, C. Knapp, M. Newman, C. Jones, Z. Chen, C. Quintana, X. Mi, A. Dunsworth, C. Gidney, I. Aleiner, F. Arute, K. Arya, J. Atalaya, R. Babbush, J. C. Bardin, R. Barends, J. Basso, A. Bengtsson, A. Bilmes, M. Broughton, B. B. Buckley, D. A. Buell, B. Burkett, N. Bushnell, B. Chiaro, R. Collins, W. Courtney, S. Demura, A. R. Derk, D. Eppens, C. Erickson, L. Faoro, E. Farhi, A. G. Fowler, B. Foxen, M. Giustina, A. Greene, J. A. Gross, M. P. Harrigan, S. D. Harrington, J. Hilton, S. Hong, T. Huang, W. J. Huggins, L. B. Ioffe, S. V. Isakov, E. Jeffrey, Z. Jiang, D. Kafri, K. Kechedzhi, T. Khattar, S. Kim, P. V. Klimov, A. N. Korotkov, F. Kostritsa, D. Landhuis, P. Laptev, A. Locharla, E. Lucero, O. Martin, M. J. R., M. McEwen, K. C. Miao, M. Mohseni, S. Montazeri, W. Mruczkiewicz, J. Mutus, O. Naaman, M. Neeley, C. Neill, M. Y. Niu, T. E. O'Brien, A. Opremcak, B. Pató, A. Petukhov, N. C. Rubin, D. Sank, V. Shvarts, D. Strain, M. Szalay, B. Villalonga, T. C. White, Z. Yao, P. Yeh, J. Yoo, A. Zalcman, H. Neven, S. Boixo, A. Megrant, Y. Chen, J. Kelly, V. Smelyanskiy, A. Kitaev, M. Knap, F. Pollmann, and P. Roushan, Realizing topologically ordered states on a quantum processor, Science **374**, 1237 (2021).
[29] G. Semeghini, H. Levine, A. Keesling, S. Ebadi, T. Wang T., D. Bluvstein, R. Verresen, H. Pichler, M. Kalinowski, R. Samajdar, A. Omran, S. Sachdev, A. Vishwanath, M. Greiner, V. Vuletić, and M. D. Lukin, Probing topological spin liquids on a programmable quantum simulator, Science **374**, 1242 (2021).
[30] X. Gu, A. F. Kockum, A. Miranowicz, Y.-X. Liu, and F. Nori, Microwave photonics with superconducting quantum circuits, Phys. Rep. **718-719**, 1 (2017).
[31] J. Q. You, X. D. Hu, S. Ashhab, and F. Nori, Low-decoherence flux qubit, Phys. Rev. B **75**, 140515 (2007).
[32] J. Koch, T. M. Yu, J. Gambetta, A. A. Houck, D. I. Schuster, J. Majer, A. Blais, M. H. Devoret, S. M. Girvin, and R. J. Schoelkopf, Charge-insensitive qubit design derived from the Cooper pair box, Phys. Rev. A **76**, 042319 (2007).
[33] E. Dagotto and T. M. Rice, Surprises on the way from one- to two-dimensional quantum magnets: The ladder materials, Science **271**, 618 (1996).
[34] P. Roushan, C. Neill, J. Tangpanitanon, V. M. Bastidas, A. Megrant, R. Barends, Y. Chen, Z. Chen, B. Chiaro, A. Dunsworth, A. Fowler, B. Foxen, M. Giustina, E. Jeffrey, J. Kelly, E. Lucero, J. Mutus, M. Neeley, C. Quintana, D. Sank,

A. Vainsencher, J. Wenner, T. White, H. Neven, D. G. Angelakis, and J. Martinis, Spectroscopic signatures of localization with interacting photons in superconducting qubits, Science **358**, 1175 (2017).

[35] Y. Ye, Z.-Y. Ge, Y. Wu, S. Wang, M. Gong, Y.-R. Zhang, Q. Zhu, R. Yang, S. Li, F. Liang, J. Lin, Y. Xu, C. Guo, L. Sun, C. Cheng, N. Ma, Z. Y. Meng, H. Deng, H. Rong, C.-Y. Lu, C.-Z. Peng, H. Fan, X. Zhu, and J.-W. Pan, Propagation and localization of collective excitations on a 24-qubit superconducting processor, Phys. Rev. Lett. **123**, 050502 (2019).

[36] Z. Yan, Y.-R. Zhang, M. Gong, Y. Wu, Y. Zheng, S. Li, C. Wang, F. Liang, J. Lin, Y. Xu, C. Guo, L. Sun, C.-Z. Peng, K. Xia, H. Deng, H. Rong, J. Q. You, F. Nori, H. Fan, X. Zhu, and J.-W. Pan, Strongly correlated quantum walks with a 12-qubit superconducting processor, Science **364**, 753 (2019).

[37] Y. E. Kraus and O. Zilberberg, Topological equivalence between the Fibonacci quasicrystal and the Harper model, Phys. Rev. Lett. **109**, 116404 (2012).

[38] D. R. Hofstadter, Energy levels and wave functions of Bloch electrons in rational and irrational magnetic fields, Phys. Rev. B **14**, 2239 (1976).

[39] C. Senko, J. Smith, P. Richerme, A. Lee, W. C. Campbell, and C. Monroe, Coherent imaging spectroscopy of a quantum many-body spin system, Science **345**, 430 (2014).

[40] P. Jurcevic, P. Hauke, C. Maier, C. Hempel, B. P. Lanyon, R. Blatt, and C. F. Roos, Spectroscopy of interacting quasiparticles in trapped ions, Phys. Rev. Lett. **115**, 100501 (2015).

[41] W. Cai, J. Han, F. Mei, Y. Xu, Y. Ma, X. Li, H. Wang, Y. P. Song, Z.-Y. Xue, Z.-q. Yin, S. Jia, and L. Sun, Observation of topological magnon insulator states in a superconducting circuit, Phys. Rev. Lett. **123**, 080501 (2019).

[42] Y. E. Kraus, Y. Lahini, Z. Ringel, M. Verbin, and O. Zilberberg, Topological states and adiabatic pumping in quasicrystals, Phys. Rev. Lett. **109**, 106402 (2012).

[43] Q. Niu and D. J. Thouless, Quantised adiabatic charge transport in the presence of substrate disorder and many-body interaction, J. Phys. A **17**, 2453 (1984).

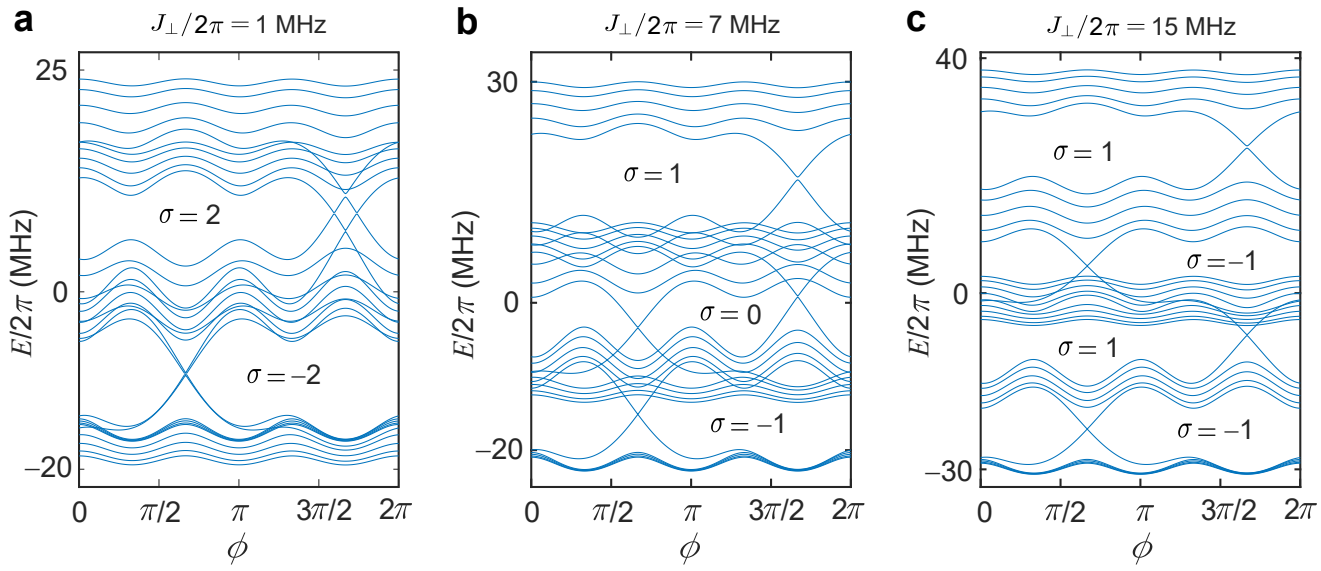
[44] R. B. Laughlin, Quantized Hall conductivity in two dimensions, Phys. Rev. B **23**, 5632 (1981).

[45] A. Fabre, J.-B. Bouhiron, T. Satoor, R. Lopes, and S. Nascimbene, Laughlin's topological charge pump in an atomic Hall cylinder, Phys. Rev. Lett. **128**, 173202 (2022).

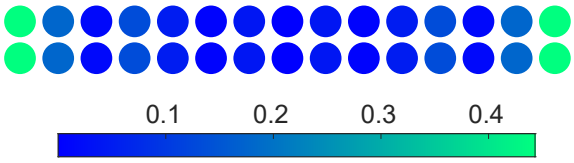
[46] Z. Fedorova, H. Qiu, S. Linden, and J. Kroha, Observation of topological transport quantization by dissipation in fast Thouless pumps, Nat. Commun. **11**, 3758 (2020).

[47] Q. Zhu, Z.-H. Sun, M. Gong, F. Chen, Y.-R. Zhang, Y. Wu, Y. Ye, C. Zha, S. Li, S. Guo, H. Qian, H.-L. Huang, J. Yu, H. Deng, H. Rong, J. Lin, Y. Xu, L. Sun, C. Guo, N. Li, F. Liang, C.-Z. Peng, H. Fan, X. Zhu, and J.-W. Pan, Observation of thermalization and information scrambling in a superconducting quantum processor, Phys. Rev. Lett. **128**, 160502 (2022).

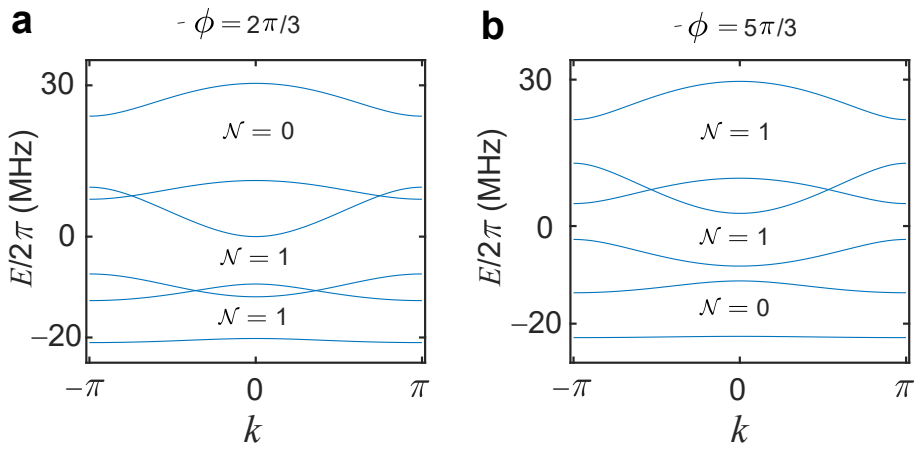
[48] S.-S. Li, Z.-Y. Ge, and H. Fan, Localization of rung pairs in a hard-core Bose-Hubbard ladder, Phys. Rev. A **102**, 062409 (2020).



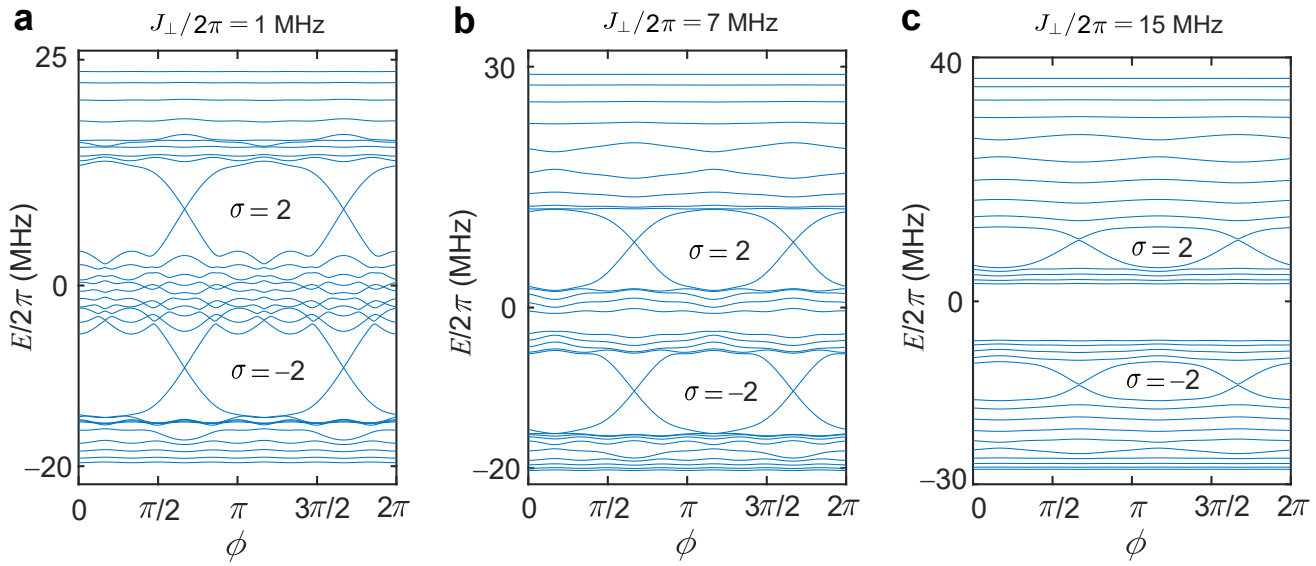
Extended Data Fig. 1. **Energy spectra for the bilayer topological system with the same periodically modulated on-site potentials. a–c**, Energy spectra versus ϕ of a finite ladder with 30 sites for the same modulated amplitudes $\Delta_\uparrow/2\pi = \Delta_\downarrow/2\pi = 12$ MHz with $J_\perp/2\pi = 1$ MHz (**a**), $J_\perp/2\pi = 7$ MHz (**b**), and $J_\perp/2\pi = 15$ MHz (**c**). Other parameters used are $J_\parallel/2\pi = 8$ MHz, $J'_\parallel = 0.1J_\parallel$, and $J_\times = 0.2J_\parallel$.



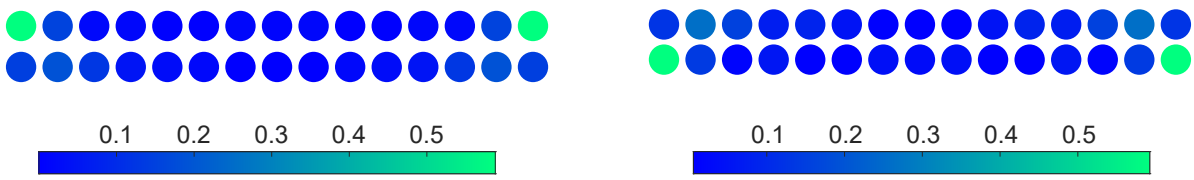
Extended Data Fig. 2. **Mid-gap state for the bilayer topological system with the same periodically modulated on-site potentials.** Density distribution of a mid-gap state for $\Delta_\uparrow/2\pi = \Delta_\downarrow/2\pi =$ 12 MHz and $\phi = \frac{2\pi}{3}$ with $J_\perp/2\pi =$ 7MHz, $J_\parallel/2\pi = 8$ MHz, $J'_\parallel = 0.1J_\parallel$, and $J_\times = 0.2J_\parallel$.



Extended Data Fig. 3. **Bloch energy bands for the bilayer topological system with the same periodically modulated on-site potentials. a**, **b**, Bloch energy bands versus k for identical chains in a qubit ladder, with modulated amplitudes $\Delta_\uparrow/2\pi = \Delta_\downarrow/2\pi = 12$ MHz with $\phi = \frac{2\pi}{3}$ (**a**), and $\phi = \frac{5\pi}{3}$ (**b**). The topological invariant $\mathcal{N}$ at each band gap is indicated, and $\mathcal{N} = 1$ indicates a pair of edge states. Other parameters used are $J_\perp/2\pi = 7$ MHz, $J_\parallel/2\pi = 8$ MHz, $J'_\parallel = 0.1J_\parallel$, and $J_\times = 0.2J_\parallel$.



Extended Data Fig. 4. **Energy spectra for the bilayer topological system with opposite periodically modulated on-site potentials. a–c**, Energy spectra versus ϕ of a finite ladder with 30 sites for opposite modulated amplitudes $\Delta_\uparrow/2\pi = -\Delta_\downarrow/2\pi = 12$ MHz with $J_\perp/2\pi = 1$ MHz (**a**), $J_\perp/2\pi = 7$ MHz (**b**), and $J_\perp/2\pi = 15$ MHz (**c**). Other parameters used are $J_\parallel/2\pi = 8$ MHz, $J'_\parallel = 0.1J_\parallel$, and $J_\times = 0.2J_\parallel$.



Extended Data Fig. 5. **Mid-gap states for the bilayer topological system with opposite periodically modulated on-site potentials.** Density distribution of mid-gap states for $\Delta_\uparrow/2\pi = -\Delta_\downarrow/2\pi = 12$ MHz and $\phi = \frac{2\pi}{3}$ with $J_\perp/2\pi = 7$ MHz, $J_\parallel/2\pi = 8$ MHz, $J'_\parallel = 0.1J_\parallel$, and $J_\times = 0.2J_\parallel$. The left panel is for a mid-gap state in the second gap; and the right panel is for a mid-gap state in the fourth gap. Note that the first and fifth gaps in Extended Data Fig. 4**b** are not clearly shown due to finite-size effects.

Supplementary Files

This is a list of supplementary files associated with this preprint. Click to download.

- suppvideo.mp4
- Supp.pdf